

# Characterization of micro-contact properties using a novel micromachined apparatus

Ben-Hwa Jang<sup>1,2</sup>, Po-Hsun Tseng<sup>3</sup> and Weileun Fang<sup>1,3</sup>

<sup>1</sup> Institute of NanoEngineering and MicroSystems, National Tsing Hua University, Hsinchu, Taiwan

<sup>2</sup> Material and Chemical Research Laboratory, Industrial Technology Research Institute, Chutung, Hsinchu, Taiwan

<sup>3</sup> Department of Power Mechanical Engineering, National Tsing Hua University, Hsinchu, Taiwan

E-mail: [fang@pme.nthu.edu.tw](mailto:fang@pme.nthu.edu.tw)

Received 10 January 2008, in final form 6 March 2008

Published 4 April 2008

Online at [stacks.iop.org/JMM/18/055020](http://stacks.iop.org/JMM/18/055020)

## Abstract

This study demonstrated a micromachined testing device consisting of two chips to characterize the micro-contact properties, such as the contact force, the contact resistance and the contact surface roughness, of metal thin films. The testing device was designed to remove the parasitic resistance during the measurement. In addition, the two chips of the testing device can be disassembled and re-assembled; the interfacial properties can be quantified at different contact cycles. Thus, both the qualitative and quantitative relationships between the interfacial properties and the contact resistance can then be investigated. To demonstrate the feasibility of the present apparatus, the contact characteristics of evaporated Al films were characterized at different contact forces and cycles. Potential applications of the present apparatus included the performance enhancement for RF-MEMS switches, micro-connectors and micro-probes.

(Some figures in this article are in colour only in the electronic version)

## 1. Introduction

Contact resistance plays an important role in determining the reliability and the integrity of transmitted electrical signals. For example, the operation and lifetime of various electromechanical devices, such as relays, switches and connectors, greatly depend on the electrical contact resistance performance. To provide sufficient contact force is an efficient way to minimize the contact resistance. This approach has been applied to various macro-scale products with contact force at the mN level [1, 2]. For micro- or nano-scale devices of  $\mu\text{N}$  or nN contact forces, it is widely recognized that parameters such as surface topography, electrical and mechanical surface properties, environmental conditions, insulating films, contact load and voltage drop play key roles in the current flow at contacting surfaces.

Various microdevices have been reported to characterize the contact resistance in small scale. The electrostatic actuated RF MEMS switch was developed to measure the relationship between the applied voltage and the contact

resistance [3]. In [4], a piezodriven device with the four-point resistance measurement device was employed to correlate the relationship between the contact resistance and contact force. The thermal actuated lateral relay (in-plane contact) made by MUMP's process was implemented to find the relationship between contact force and the contact resistance [5]. The electrostatic actuated bridge-type microdevice was used in [6] to remove ultrathin native oxide films at contact interfaces by nondestructive electromechanical means. The four-point resistance measurement device driven by an atomic force microscope (AFM) was employed to characterize the contact resistance [7]. The contact properties of cantilever beam style RF MEMS switches were characterized using the nano-indenter in [8, 9]. The non-contact laser profiler was used to determine the relationship between contact force and contact area [10]. Moreover, theoretical works have been extensively studied to model contact resistance in small scale [11–13].

However, little has been known about the influence of interfacial properties on measurement results with multiple contact cycles. Due to the limitations of micro-scale

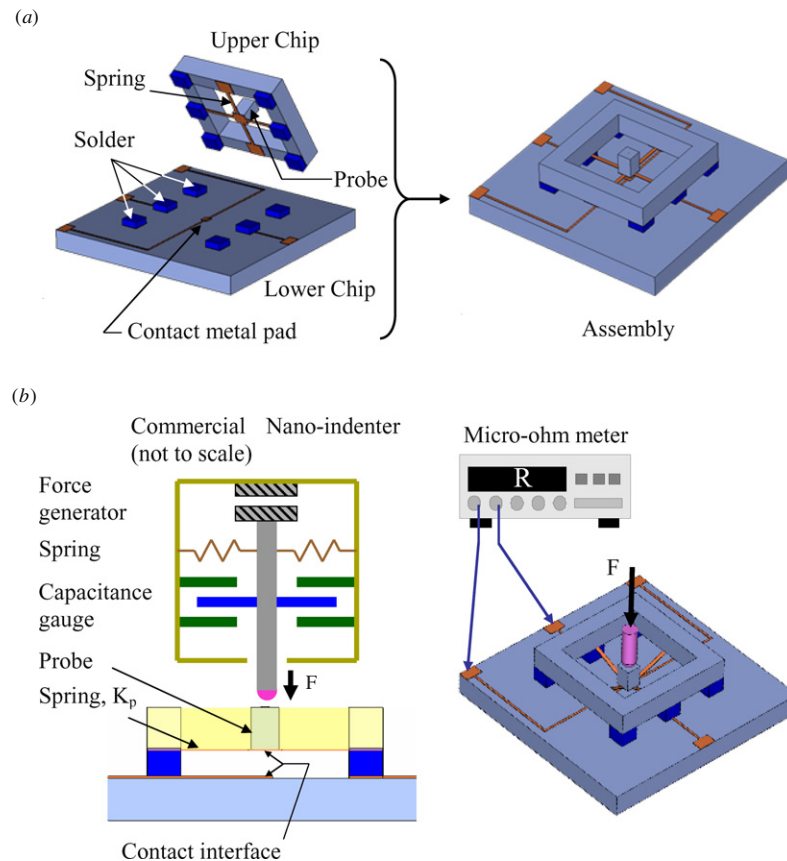


**Figure 1.** The schematic of the present (a) testing device, and (b) experimental setup. The testing device is composed of an upper chip and a lower chip. The experimental setup consists of a micro-ohm meter, a nano-indenter and a testing device.

device fabrication, methods to precisely extract the interfacial properties such as the contact force, the contact resistance and the surface roughness at various contact cycles have also not been well explored. This study presented a novel on-chip apparatus integrated with a commercial nano-indenter and an AFM to characterize Al–Al contact properties. The chips of the apparatus were designed to be easily disassembled for each testing, and thus the surface roughness at each contact cycle can be measured. Since our unique circuit routing enabled the parasitic resistance on chips of the apparatus to be eliminated, the constriction resistance can be obtained more precisely. Thus, the cause–effect relations between the interfacial properties and the constriction resistance can be investigated.

## 2. Design of the test apparatus

As illustrated in figure 1(a), the testing device was composed of the upper chip and the lower chip. The upper chip contained a micromachined probe with the testing metal coated on its tip and supported by four springs. The stiffness of the springs  $K_p$  prevented shorting before the contact test. The lower chip also contained the metal pad to be tested. The transparent glass was used as the substrate of the lower chip for the ease of assembly. The upper chip and the lower chip were then

bonded by the solder. The alignment was improved by the self-aligning characteristic of solder reflow. Nevertheless, to avoid the misalignment at contact area, the planar dimensions of the micromachined probe ( $300 \mu\text{m} \times 300 \mu\text{m}$ ) at the upper chip were designed to be much larger than that of the metal pad ( $50 \mu\text{m} \times 50 \mu\text{m}$ ) at the lower chip. The solder also acted as a spacer and an electrical interconnect between these two chips. The experimental setup, as shown in figure 1(b), consisted of a micro-ohm meter, a nano-indenter and a testing device. The nano-indenter was used to apply load on the probe at the upper chip, so as to move the probe tip to contact with the metal pad on the lower chip. The contact force was precisely specified and tuned by the force generator of the nano-indenter during test. Meanwhile, the displacement of the probe was recorded by the capacitance gauge of the nano-indenter. The contact resistance can be read from the micro-ohm meter using the constant current mode. Since it was easy to separate the upper chip and the lower chip by reflowing solder, the variation of the contact surface roughness before and after each contact test can be characterized using the AFM. Consequently, the testing device can be employed to explore the relationship among the contact force, the contact resistance and the contact surface roughness at various contact cycles.

The contact interface is critical for the evaluation of the contact resistance. The surface roughness, the surface insulating film and the contamination in the contact interface

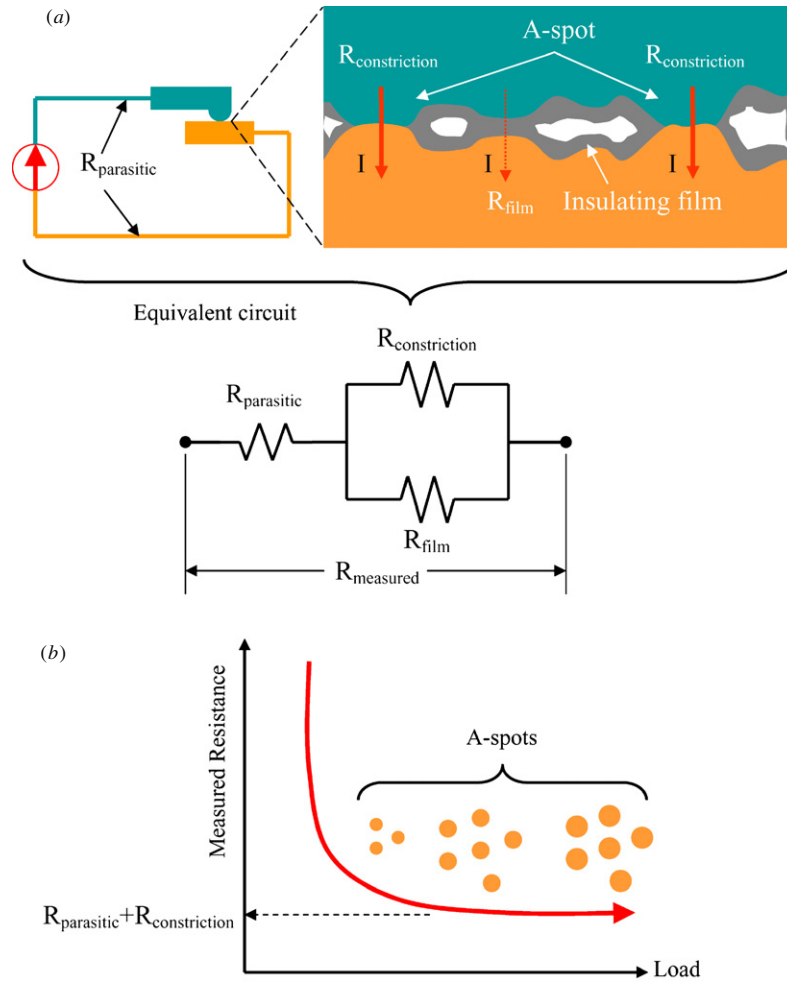


**Figure 2.** Two rough surfaces in normal contact: (a) schematic illustration and the equivalent circuit at the contact interface, and (b) the relationship between the contact resistance and normal load. With increasing contact loads,  $F$ , the contact area or the number of A-spots increases and the constriction resistance decreases. Due to the work-hardening of the A-spots, the deformed rate of the A-spots will be decreased and the contact resistance will converge to  $R_{\text{parasitic}} + R_{\text{constriction}}$ .

may influence the contact resistance. The effective contact area, named asperities or A-spots, is usually a small fraction of the total contact area [2, 14, 15]. The number and the size of A-spots depend primarily on surface roughness, material hardness and the magnitude of the normal contact force. Figure 2(a) is a schematic diagram showing the contact interface between two rough surfaces with insulating films. The constriction of current flow will occur in the region of each A-spot, so as to lead to a constriction resistance,  $R_{\text{constriction}}$ . In addition, the contact region of two insulating films has a film resistance,  $R_{\text{film}}$ . While increasing the contact load  $F$ , the size and the number of A-spots are increased and thus the constriction resistance is decreased. However, due to the work-hardening of the metal material near the contact area, the deformation rate of A-spots will be decreased, and therefore the contact resistance will converge to a particular value, as shown in figure 2(b) [15]. Referring to the model in figure 2(a), the measured resistance consisted of the parasitic resistance of the testing device and the resistance at the contact interface. Before the formation of A-spots, the constriction

resistance  $R_{\text{constriction}}$  is infinity and the measured resistance can be expressed as

$$R_{\text{measured}} = R_{\text{parasitic}} + R_{\text{film}}. \tag{1}$$

However, after the formation of A-spots, the measured resistance becomes

$$R_{\text{measured}} = R_{\text{parasitic}} + \frac{R_{\text{film}} \cdot R_{\text{constriction}}}{R_{\text{film}} + R_{\text{constriction}}}. \tag{2}$$

In general, the film resistance  $R_{\text{film}}$  is very large as compared with the constriction resistance, and therefore equation (2) can be rewritten as

$$R_{\text{measured}} = R_{\text{parasitic}} + R_{\text{constriction}}. \tag{3}$$

As a result, referring to equations (1) and (3), the film resistance as well as the constriction resistance can be determined by the calibrated resistance:

$$R_{\text{calibrated}} = R_{\text{measured}} - R_{\text{parasitic}}. \tag{4}$$

This study presented a novel calibration method, as shown in figure 3, to eliminate the parasitic resistance of the testing apparatus. Thus, based on equation (3), the

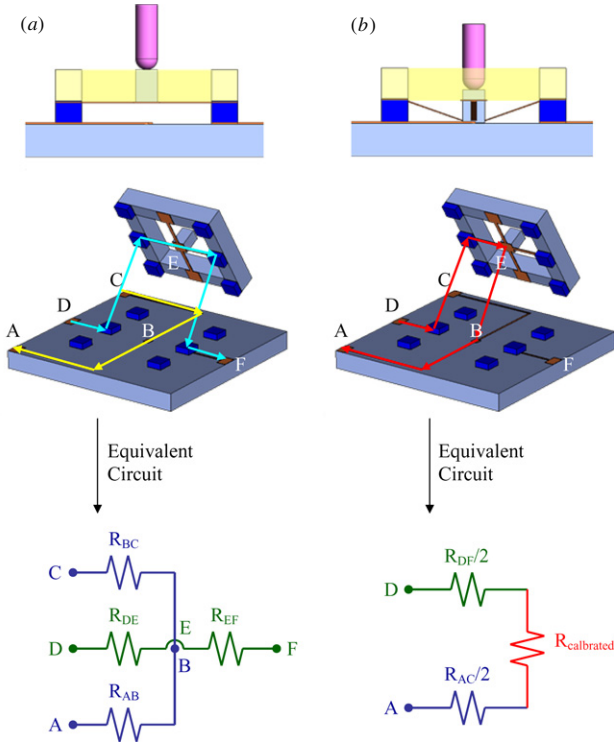


**Figure 3.** The calibration method for the parasitic resistance and its equivalent circuit (a) before and (b) after loading by the nano-indenter. Before loading, due to the symmetrical routing, the parasitic resistance  $R_{AB} = R_{BC} = R_{AC}/2$  was determined by measuring the resistance  $R_{AC}$  and so was the parasitic resistance  $R_{DE} = R_{EF} = R_{DF}/2$  by measuring the resistance  $R_{DF}$ . After loading, points B and E were electrically short; the parasitic resistance was  $R_{AB} + R_{DE} = (R_{AC} + R_{DF})/2$  by measuring the resistance  $R_{AD}$ .

constriction resistance at various contact conditions can be measured. Prior to the loading of the nano-indenter, the parasitic resistances  $R_{AB}$  and  $R_{BC}$  can be determined by measuring the resistance  $R_{AC}$  (between points A and C) in figure 3(a). Due to the symmetrical routings,  $R_{AB} = R_{BC}$  were equal to  $R_{AC}/2$ . Similarly, the parasitic resistances  $R_{DE}$  and  $R_{EF}$  can be determined by measuring the resistance  $R_{DF}$  (between points D and F), and  $R_{DE} = R_{EF} = R_{DF}/2$ . The equivalent circuit was also available in figure 3(a). During the test, the metal tip will be driven by the nano-indenter to contact with the metal pad, and points B and E were electrically short, as shown in figure 3(b). In this case, the measured resistance was  $R_{AD}$ , and the parasitic resistance was  $(R_{AC} + R_{DF})/2$ ; thus, the calibrated resistance was

$$R_{\text{calibrated}} = R_{AD} - \frac{R_{AC}}{2} - \frac{R_{DF}}{2}, \quad (5)$$

and the equivalent circuit is shown in figure 3(b).

To demonstrate the present approach, the contact properties of the Al film were characterized. This study established the fabrication processes outlined in figures 4(a) and (b) to implement the upper chip and the lower chip, respectively. As illustrated in figure 4(a), a silicon wafer was thermally oxidized first and then deposited with 2  $\mu\text{m}$  thick poly-silicon using low-pressure chemical vapor deposition

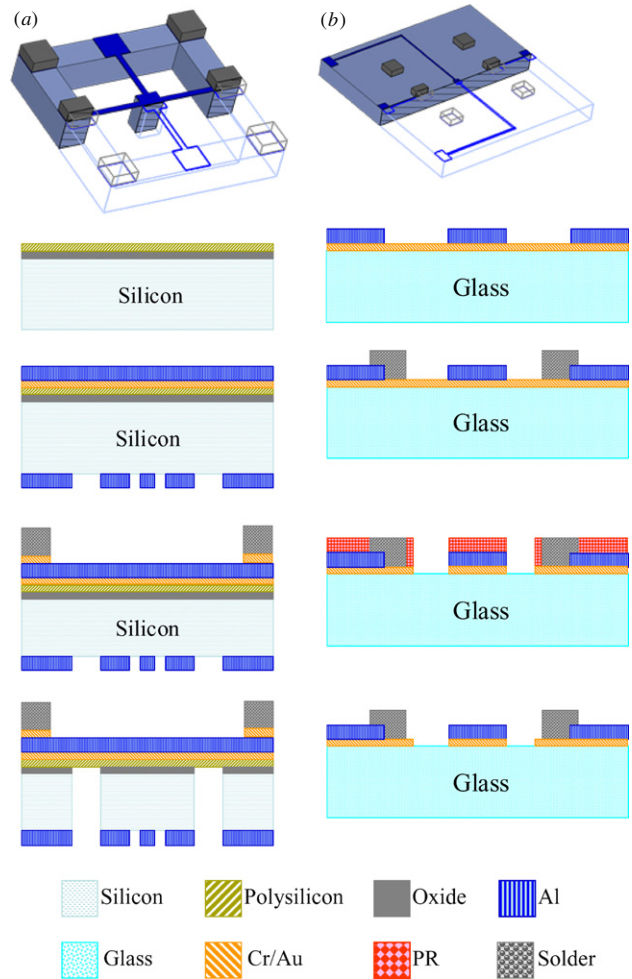


**Figure 4.** Illustration of the fabrication steps for (a) the upper chip (on silicon), and (b) the lower chip (on glass).

(LPCVD). The poly-silicon was patterned to define the springs and the probe. After that, a 1.8  $\mu\text{m}$  thick Al film was deposited and patterned on the top of the poly-silicon layer to act as the metal wiring and the contact pad. The Al film was also patterned on the backside of the wafer to act as a hard mask for the following deep reactive ion etching (DRIE). Solders of 17  $\mu\text{m}$  thickness were patterned and electroplated with Cr/Au as the seed layer. The silicon probe was formed after the through wafer DRIE; meanwhile alignment marks for the positioning of the nano-indenter was also defined on the probe. Finally, the silicon probe and poly-silicon springs were released from the substrate after the oxide being removed by RIE. As shown in figure 4(b), the lower chip was evaporated with Cr/Au as a seed layer. A 1  $\mu\text{m}$  thick Al film was deposited and patterned to define conductive wires, solder pads and the contact metal pad. Solders of 17  $\mu\text{m}$  thickness were electroplated to form the spacer between the upper chip and the lower chip. Finally, the upper chip and the lower chip were bonded by solder reflowing on the hot plate of 300  $^{\circ}\text{C}$  for 5 min to form the testing device for the contact test. On the other hand, it was also easy to disassemble and re-assemble the chips of the testing device by heating during the contact

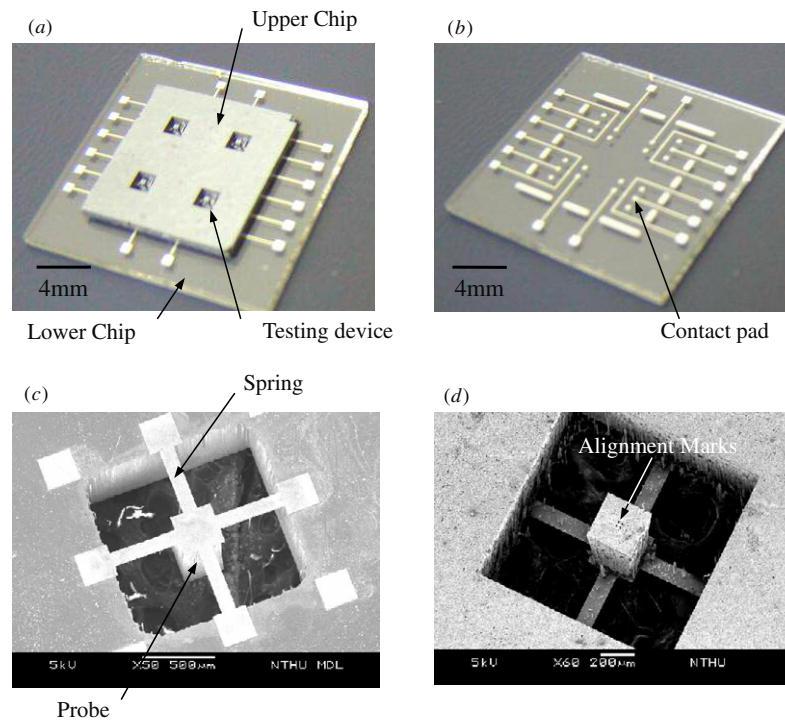


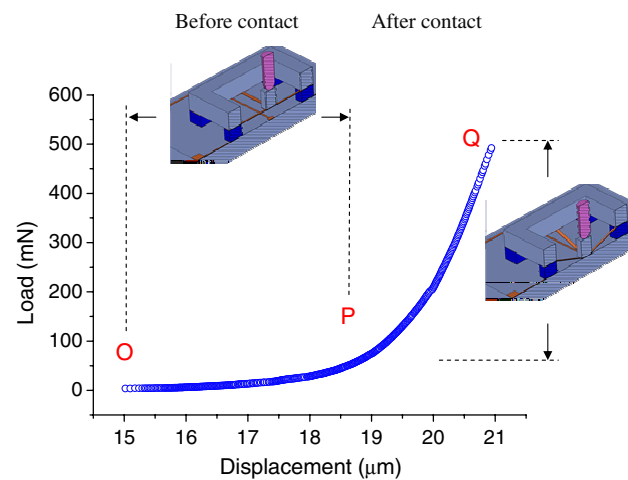
**Figure 5.** Photographs of (a) the whole test device consisting of the upper chip and the lower chip, and (b) the lower chip. (c)–(d) SEM micrographs of the top and bottom views of the upper chip.

test. Thus, the variation of the surface roughness of the tested Al film with the contact force as well as the contact cycle can be characterized.

### 3. Experiment results and discussions

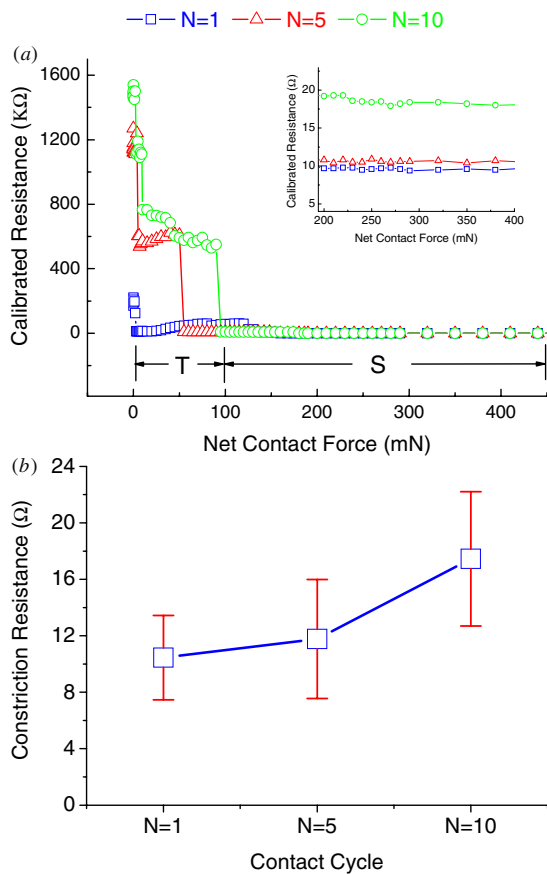
Figure 5 shows photos of the typical fabricated devices. The photo in figure 5(a) shows the assembled testing unit after the bonding of the upper chip and the lower chip. In this study, each testing unit was composed of four testing devices for the contact resistance test. The photo in figure 5(b) shows the lower chip, and the distribution of the metal wires, the solder pads and the contact pads are clearly observed. The zoom-in SEM photos in figures 5(c) and (d) show the top and bottom views of the upper chip, respectively. The silicon probe and poly-silicon springs were demonstrated in these photos. In this case, the spring  $K_p$  was  $500 \mu\text{m}$  long and  $60 \mu\text{m}$  wide, and the planar dimensions of the probe tip were  $300 \mu\text{m} \times 300 \mu\text{m}$ . Figure 5(d) also shows the alignment marks to ensure the load from the nano-indenter applying at the center of the probe.

Figure 6 shows the output load and displacement recorded by the nano-indenter during contact test. As shown in figure 6, the indenter tip did not touch the probe until it reached point O. After that, a bilinear relationship was observed between output load and displacement of the nano-indenter. The section OP represented that the probe of the upper chip moved downward by the nano-indenter, but not yet contacted with the pad on the lower chip. Thus the slope of OP indicated the stiffness of the springs  $K_p$  and the value was  $7.77 \text{ mN } \mu\text{m}^{-1}$ . The



**Figure 6.** The load versus displacement measured by the nano-indenter during the contact test. The slope of OP indicated the stiffness of the springs. The section PQ indicated the variation of the contact force between the probe and the contact pad.

total restoring force of supporting springs from  $K_p$  can be determined from the displacement of the probe. Near point P, the probe on the upper chip initially touched the contact pad on the lower chip, causing the dramatic increase in the slope of the force–displacement curve. Thus, the section PQ further indicated the variation of the contact force between the probe and the contact pad. The net contact force on the contact surface can be determined by subtracting the total restoring



**Figure 7.** (a) The net contact force versus the calibrated resistance during the contact test for different  $N$ , and (b) the relationship between the constriction resistance and the contact cycle in the stable region. In the transition region T, the plateau of the calibrated resistance curve attributed to the native oxide film formed on the contact interface. In the stable region S, the measured calibrated resistance revealed the constriction resistance.

force of supporting springs from the output load of the nano-indenter.

The contact test was performed on three different samples under the conditions of the ambient temperature of 25 °C and relative humidity of 70%. A thin native oxide ( $\text{Al}_2\text{O}_3$ ) is often grown on the aluminum contact surface. The measured parasitic resistances  $R_{AC}$  and  $R_{DF}$  shown in figure 3 were  $5.93 \pm 0.08 \Omega$  and  $7.71 \pm 0.24 \Omega$ , respectively, and then the calibrated resistance was further determined from equation (5). For each sample, the variation of the calibrated resistance with the net contact force was characterized at  $N = 1$  first. The sample was then debonded to measure the surface roughness of the contact interface. After that, the upper chip and the lower chip were bonded again to measure the calibrated resistance versus the net contact force at  $N = 5$ . The debonding, bonding and contact test will be repeated again for  $N = 10$ . The typical relationships between the calibrated resistance and the net contact force were characterized at three different contact cycles  $N$  ( $N = 1, 5$  and  $10$ ), as shown in figure 7(a). In general, the calibrated resistance decreased with the increase of the net contact force. The measurement

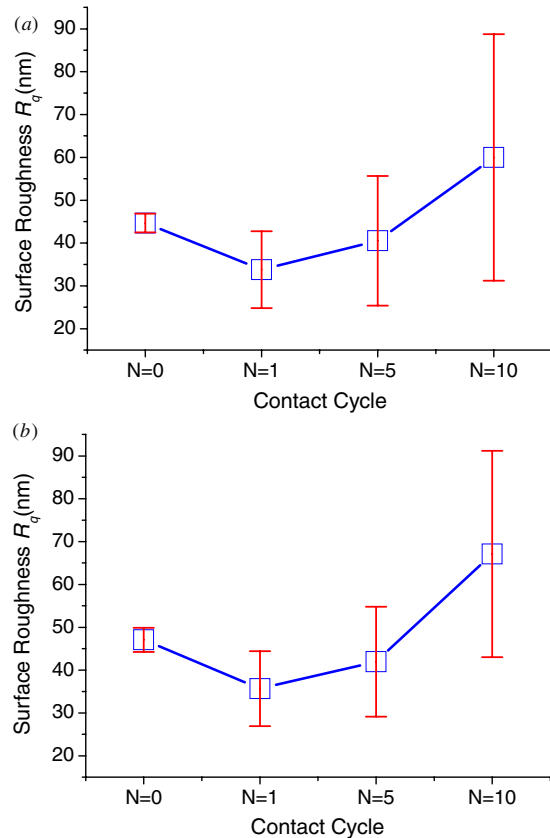


**Figure 8.** The contact surface roughness  $R_q$  measured by an AFM at different contact cycles for (a) the upper chip, and (b) the lower chip.

results were categorized as a transition region T and a stable region S. In the transition region T, the plateau of the calibrated resistance curve attributed to the native oxide film formed on the contact interface. Due to the quantum tunneling effect, electrons can pass through the oxide film, resulting in tunneling current. The voltage–current characteristic of tunneling junctions represents the tunneling resistance of the oxide film. Thus, the tunneling resistance is very sensitive to the distribution of the oxide film thickness at the contact area [14]. Due to the change in surface topography of the oxide film during the compressing process, the tunneling resistance may change irregularly as the net contact force increased in the transition region (i.e. the calibrated resistance was even slightly increased with the increase of the net contact force for  $N = 1$  and  $N = 5$ ). As the contact force increased, the native oxide film was broken and the A-spots were established at the contact interface. This caused the drastic decrease in the calibrated resistance [8]. On the other hand, in the stable region S, the measured calibrated resistance revealed the constriction resistance and had no significant change with the contact force. Moreover, it was also obtained that the case with larger contact cycles had a higher constriction resistance in the region S. The relationship between the constriction resistance and the contact cycle in the stable region is summarized in figure 7(b).

Figures 8(a) and (b) show the variation of the surface roughness for the upper chip and the lower chip measured

by the AFM at different contact cycles. With the mechanical load, the contact surface roughness on either the upper chip or the lower chip was small at the first cycle ( $N = 1$ ). However, the roughness of the contact surface is increased with increasing contact cycles ( $N = 5-10$ ). This may be due to the increase of contact-produced debris trapped at the interface with increasing contact cycles [6, 16]. These results support the characteristic shown in figure 7(b). In short, the increase of the surface roughness at larger contact cycles (from  $N = 1$  to  $N = 10$ ) will lead to the increase of the constriction resistance. The increase of the standard deviation of the surface roughness with increasing contact cycles could be resulted from the misalignment during the bonding and de-bonding process of the upper chip and the lower chip.

#### 4. Conclusions

In this paper, a novel testing device consisting of two micro fabricated chips was successfully implemented. The testing device integrated with a commercial nano-indenter for directly measuring the relationship between the contact resistance and the contact force. To improve the accuracy of measurement, the electrical routings on the testing device were specially designed to eliminate the parasitic resistance, and consequently the constriction resistance can be measured. Since the two chips of the testing device can be disassembled and re-assembled, the interfacial properties can be readily quantified at different contact cycles. Thus, both the qualitative and quantitative relationships between the interfacial properties and the contact resistance can then be investigated. To demonstrate the feasibility of the present apparatus, the contact characteristics of evaporated Al films were characterized at different contact forces and cycles. The proposed on-chip apparatus provides a foundation for extracting more quantitative information for future micro-contact investigations. Many applications can be explored such as enhancing the performances of RF-MEMS switches, micro-connectors and probe cards.

#### Acknowledgments

This project was (partially) supported by the NSC of Taiwan under grant of NSC 95-2218-E-007-024 and by the MOEA of Taiwan under grant of 6301XSY5H1. The authors would also like to thank the Center for Nano-Science and Technology of National Tsing Hua University, the Nano Facility Center of

National Chiao Tung University and the NEMS research center of National Taiwan University in providing the fabrication facilities.

#### References

- [1] Liu W and Pecht M 2004 *IC Component Sockets* (New York: Wiley)
- [2] Mroczkowski R S 1998 *Electronic Connector Handbook: Theory and Applications* (New York: McGraw-Hill)
- [3] Majumder S, McGruer N E, Zavracky P M, Adams G G, Morrison R H and Krim J 1997 Measurement and modeling of surface micromachined, electrostatically actuated microswitches *Transducers '97 (Chicago, IL)* pp 1145-8
- [4] Schimkat J 1999 Contact measurements providing basic design data for microrelay actuators *Sensors Actuators A* **73** 138-43
- [5] Kruglick E J J and Pister K S J 2000 Lateral MEMS microcontact considerations *J. Microelectromechan. Syst.* **8** 264-71
- [6] Kogut L and Komvopoulos K 2005 Breakdown of ultrathin native oxide films at contact interfaces of electromechanically stressed silicon microdevices *J. Appl. Phys.* **97** 124102
- [7] DeNatale J, Mihailovich R and Waldrop J 2002 Techniques for reliability analysis of MEMS RF switch *40th Int. Reliability Physics Symp. (Dallas, TX)* pp 116-7
- [8] Coutu Jr R A, Kladitis P E, Starman L A and Reid J R 2004 A comparison of micro-switch analytic, finite element, and experimental results *Sensors Actuators A* **115** 252-8
- [9] Lee H, Coutu Jr R A, Mall S and Kladitis P E 2005 Nanoindentation technique for characterizing cantilever beam style RF microelectromechanical systems (MEMS) switches *J. Micromech. Microeng.* **15** 1230-5
- [10] McBride J W 2006 The loaded surface profile: a new technique for the investigation of contact surfaces *5th Int. Conf. on Entertainment Computing (Cambridge, UK)* pp 150-6
- [11] Rudzitis J, Padamans V, Bordo E and Haytham R 1998 Random process model of rough surfaces contact *Meas. Sci. Technol.* **9** 1093-7
- [12] Boyer L 2001 Contact resistance calculations: generalizations of Greenwood's formula including interface films *IEEE Trans. Comp. Packag. Technol.* **24** 50-8
- [13] Kogut L and Komvopoulos K 2004 Electrical contact resistance theory for conductive rough surfaces separated by a thin insulating film *J. Appl. Phys.* **95** 576-85
- [14] Holm R 2000 *Electric Contacts: Theory and Applications* 4th edn (Berlin: Springer)
- [15] Slade P G 1999 *Electrical Contacts: Principles and Applications* (New York: Dekker)
- [16] Jensen B D, L-W Chow L, Huang K, Saitou K, Volakis J L and Kurabayashi K 2005 Effect of nanoscale heating on electrical transport in RF MEMS switch contacts *J. Microelectromechan. Syst.* **14** 935-46